AGU PUBLICATIONS

JGR

Journal of Geophysical Research: Oceans

RESEARCH ARTICLE

10.1002/2015JC011594

Direct observations of the Antarctic Slope Current transport at 113°E

B. Peña-Molino[1], M. S. McCartney[2], and S. R. Rintoul[1,3,4]

[1]Antarctic Climate and Ecosystem Cooperative Research Centre, University of Tasmania, Hobart, Tasmania, Australia, [2]Woods Hole Oceanographic Institution, Woods Hole, Massachusetts, USA, [3]CSIRO Marine and Atmospheric Research, Hobart, Tasmania, Australia, [4]Centre for Weather and Climate Research, Hobart, Tasmania, Australia

Key Points:
- The mean transport of the Antarctic Slope Current (ASC) is −29.2 Sv
- Mean and variability of the ASC are predominantly barotropic
- Variability is due to open ocean eddy processes and wind forcing through changes in the Antarctic Slope Front

Correspondence to:
B. Peña-Molino,
beatriz.penamolino@utas.edu.au

Citation:
Peña-Molino, B., M. S. McCartney, and S. R. Rintoul (2016), Direct observations of the Antarctic Slope Current transport at 113°E, *J. Geophys. Res. Oceans*, *121*, 7390–7407, doi:10.1002/2015JC011594.

Received 21 DEC 2015
Accepted 16 SEP 2016
Accepted article online 21 SEP 2016
Published online 12 OCT 2016

Abstract The Antarctic Slope Current (ASC), defined here as the region of westward flow along the continental slope off Antarctica, forms the southern limb of the subpolar gyres. It regulates the exchange of water across the shelf break and provides a path for interbasin westward transport. Despite its significance, the ASC remains largely unobserved around most of the Antarctic continent. Here we present direct velocity observations from a 17 month current meter moored array deployed across the continental slope between the 1000 and the 4200 m isobaths, in the southeastern Indian Ocean near 113°E. The observed time-mean flow consists of a surface-intensified jet associated with the Antarctic Slope Front (ASF) and a broader bottom-intensified westward flow that extends out to approximately the 4000 m isobath and is strongest along the upper slope. The time-mean transport of the ASC is −29.2 Sv. Fluctuations in the transport are large, typically exceeding the mean by a factor of 2. They are mainly due to changes in the northward extent of the current over the lower slope. However, seasonal changes in the wind also drive variations in the transport of the ASF and the flow in the upper slope. Both mean and variability are largely barotropic, thus invisible to traditional geostrophic methods.

1. Introduction

The Antarctic Slope Current (ASC) is a more or less continuous band of westward flow that surrounds most of the Antarctic continent. In the Weddell Sea, the Ross Sea and the Indian Ocean sector the ASC forms the southern limb of the subpolar gyres. It owes its presence to the predominantly easterly winds around Antarctica. These winds drive an Ekman transport to the south; the geostrophic adjustment of the waters below the Ekman layer is responsible for the observed westward flow. However, across the broad region of westward flow that defines the ASC, the isopycnal tilt is gentle and often upward toward the south, as a result of the upwelling driven by the divergence of the winds south of the Antarctic Circumpolar Current (ACC). The geostrophic shear associated with a positive slope in the isopycnals is also positive, consistent with surface-intensified eastward flow. Despite this positive shear around much of the Antarctic continent, models and observations consistently show westward flow along the continental slope, indicating that the ASC has a strong barotropic component to the west that is opposite sign to the shear. This barotropic nature of the ASC is not surprising, since the wind stress curl south of the ACC is negative, and the response of a weakly stratified ocean to such forcing is in the form of a barotropic cyclonic gyre [*Morrow et al*., 2008].

Embedded in this broad zone of westward transport are several narrow frontal currents. Near the shelf break the predominant feature is the Antarctic Slope Front (ASF), a sharp density front in the upper 500 m of the water column separating the warmer ocean to the north from the cold and fresh shelf waters to the south [*Jacobs*, 1991; *Whitworth et al*., 1998]. In contrast to deeper waters, isopycnals slope downward toward the south across the front (Figure 1), resulting in the large negative geostrophic shear, the ASF contributes to the ASC. In areas where dense water is formed, the presence of the dense water on the shelf leads to a V-shaped structure in the density field that is often seen around Antarctica [*Gill*, 1973].

Coupled to this horizontal circulation, a vertical and meridional circulation across the ASC regulates the exchange of properties between the deep ocean and the Antarctic shelves. In areas where the ASC is absent, as is the case along the West Antarctic Peninsula and the Amundsen and Bellingshausen Seas, warm Circumpolar Deep Water (CDW) is directly in contact with the shelf break [*Orsi et al*., 1995] and can

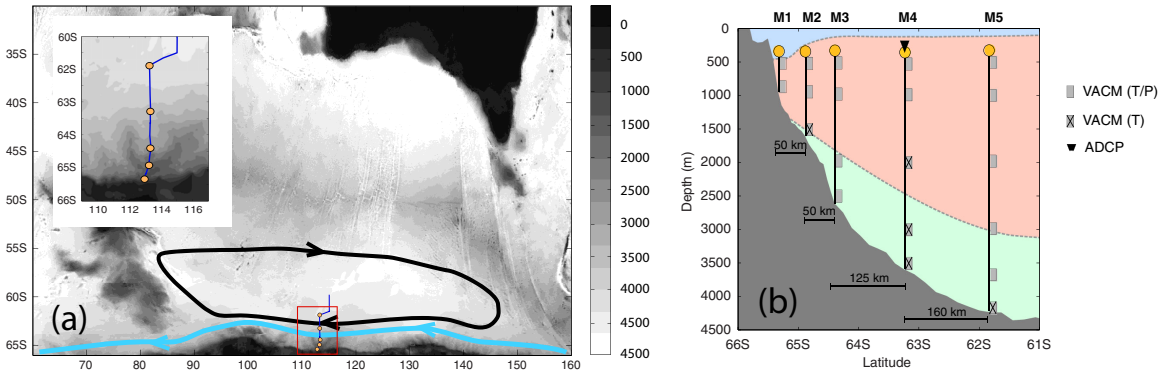

Figure 1. (a) Map of the study area showing bathymetry. Yellow circles indicate the location of the moorings, and the blue line the track followed during the recovery cruise. The circulation in the region (after MD07) is illustrated by the thick lines, with light blue showing the ASC flow that continues west of Kerguelen Plateau, and the black line the recirculation into the subpolar gyre. Inset showing detailed bathymetry around moored array [from *Arndt et al*., 2013]. (b) Schematic of the moored array design, showing instrument depth and location across the continental slope. The gray dashed lines show the location of the 0°C isotherm separating cold fresh shelf waters on top (blue), warmer and saline CDW at mid depth (red), and AABW at the bottom (green).

access the shelf with little difficulty, reaching the base of the glaciers and driving basal melt of floating ice shelves [*Shepherd et al*., 2004; *Jacobs et al*., 2011]. In addition, the ASC also mediates the formation and export of Antarctic Bottom Water (AABW), by both bringing the CDW in contact with dense shelf water, as well as allowing the AABW to reach the deep ocean. Observations suggest that changes in AABW formation [*Purkey and Johnson*, 2012] and melting of the ice shelves by CDW [*Pritchard et al*., 2012] are already occurring. Recently, models and observations have shown that interactions between the mean flow and variations in the along-shelf geometry [*Dinniman et al*., 2011; *St-Laurent et al*., 2013] as well as the eddy component of the overturning [*Nøst et al*., 2011; *Thompson et al*., 2014; *Stewart and Thompson*, 2015] are the main mechanisms regulating the water exchange across the Antarctic shelf break.

However, long-term observations over the Antarctic continental slope are still limited. Remote sensing provides little information, as the area is often covered by ice and under thick cloud cover. In situ measurements of the ASC have been collected at some of the more commonly studied areas along the Antarctic margin, namely the Weddell, Ross, and Amundsen Seas. In the Weddell Sea a great deal of effort was dedicated to quantify the transport of the subpolar gyre. Early estimates based on a Sverdrup calculation predicted a transport of 76 Sv (1 Sv $= 10^6$ m^3 s^{-1}) [*Gordon et al*., 1981], while estimates based on synoptic observations across the gyre placed the transport in the range of 20–56 Sv a decade later [*Fahrbach et al*., 1991]. More recently, *Klatt et al*. [2005] used current meter data to reference a geostrophic calculation based on several synoptic sections across the gyre at the Prime Meridian. Their results suggest along its southern limb the Weddell gyre carries 56 Sv to the west. Efforts in the Ross Sea have focused on the export of AABW [*Gordon et al*., 2009]. While observations in the Amundsen Sea have shown that the inflow of warm water driving the rapid thinning of the ice shelves is due to both wind and buoyancy forcing [*Wåhlin et al*., 2013].

In the Indian Ocean sector the existence of westward flow along the continental slope has long been known from the westward path of drifting icebergs [*Tchernia and Jeannin*, 1980; *Aoki et al*., 2010], the spreading of Antarctic Bottom water [*Orsi et al*., 1999], and the circulation of surface drifters [*Bindoff et al*., 2000]. However, the paucity of observations has made estimates of the ASC transport much more challenging. Geostrophic calculations by *Bindoff et al*. [2000] between 80 and 150°E gave ASC transports of −10 to −55 Sv, with a mean across eight sections of −29.4 Sv. Part of the ASC's westward flow in this sector was known to diverge into a deep western boundary current along the eastern flank of the Kerguelen Plateau [*Speer and Forbes*, 1994; *Donohue et al*., 1999]. A more complete geostrophic calculation to characterize the circulation of the entire Australian-Antarctic Basin subpolar gyre was carried out by [*McCartney and Donohue*, 2007, hereafter MD07]. The calculation was based on hydrographic and direct velocity measurements (both shipboard and lowered acoustic Doppler current profilers) along World Ocean Circulation Experiment (WOCE) lines I8S and I9S approximately located at 90 and 115°E. In their study they estimated the southern limb of the subpolar gyre in the Indian Ocean as −76 Sv. This strong westward flow had, according to the authors, remained elusive both due to its barotropic nature as well as the fact that it occupies latitudes typically covered by ice, and was often left unobserved. Nevertheless, evidence of the western flow of the gyre existed.

Moored observations collected while the MD07 analysis was underway confirmed the deep western boundary current along the eastern side of Kerguelen Plateau earlier noted by *Speer and Forbes* [1994], and revealed a strong bottom-intensified northward flow, with time-mean velocities near the bottom in excess of 20 cm s^{-1} and total northward transport of AABW (potential temperature $< 0°C$) of 12.3 Sv [*Fukamachi et al*., 2010]. Part of the ASC flow in MD07 fed this deep western boundary current, while the rest continued westward in the gap between the Kerguelen Plateau and Antarctica, where *Heywood et al*. [1999] estimated a −45 Sv transport. However, in the MD07 discussion of the large ASC transport estimate that emerged from their study, the authors remarked that such large transport could result from the accumulation of errors and application of various constraints and the true strength of the ASC lie somewhere around 50 Sv.

Motivated by the potential existence of such a vigorous current along the continental slope, and the considerable uncertainty of its strength, an array of current meters was deployed at the southern end of the WOCE hydrographic section I9S used by MD07. The experiment aimed to measure, for the first time, the vertical and horizontal structure of the ASC for a long enough period to estimate its mean transport, and quantify the contribution of both shear and barotropic components. Along with the structure and transport of the mean ASC, we also characterize the main modes of variability in the flow and discuss the possible forcing mechanisms behind them. While most of the general features of the circulation described by MD07 are found in the data, their time-mean amplitudes, we will show, are much less.

2. Data

2.1. The Measurements

Five moorings were deployed on the continental slope between the 1000 and the 4200 m isobaths. The array was aligned roughly across the local bathymetry, running along a more or less meridional line centered near 113°E between 65°20′S and 61°50′S at the southern end of WOCE line I9S (Figure 1). The moorings were equipped with a total of 20 Vector Averaging Current Meters (VACM) distributed between 500 m depth and the bottom, at intervals ranging from 500 to 1000 m. The instruments were set to record 30 min average horizontal velocity vectors for the duration of the experiment. The VACMs were also equipped with temperature sensors and 15 of them were equipped with pressure sensors, also providing 30 min average data. At the fourth site, located approximately on the 3500 m isobath, the array was complemented by an upward looking Acoustic Doppler Current Profiler (ADCP), extending the observations from 500 m to near the surface.

Moorings located on the upper slope, between the 1000 and the 2500 m isobaths, were separated by approximately 50 km, while the distance between the deeper moorings was approximately 125 and 160 km. The spacing between the moorings was determined by both the requirement to sample all the way out to the returning eastward flow of the cyclonic gyre, expected somewhere offshore of the 3500 m isobath (MD07), and the need to do so with a modest number of instruments. However, small-scale structure in the flow is likely to exist that is not resolved by the array due to the large spacing between moorings. We will return to this resolution issue later.

The moorings were deployed from the icebreaker Aurora Australis in December 2009, and recovered in January 2012, a year later than originally planned due to a medical emergency during the 2010–2011 field season. The majority of the instruments successfully collected data for the whole duration of the experiment. However, a number of instruments produced no usable data, mainly due to failed electronics, rotors, or other mechanical failures. Short data gaps resulting from minor instrument failure were filled by linear interpolation. The overall data return for velocity was 72%. For more details on the specific instruments the reader is referred to Table 1.

Although the majority of instruments recorded for at least 2 years, the top instruments at M2 and M3 only operated for 17 months. The record at 1000 m in M3 failed after 350 days, but we extended the time series to 17 months via linear interpolation of the instruments at 500 m and the bottom. We tested this extrapolation on the first 350 days of the record, and found had no effect on our results. Our analysis makes use of these first 17 months of data. Basic statistics for the 17 month records of zonal and meridional velocities are provided in Table 2. These include mean scalar speeds and standard deviations to show that the VACMs spent most of their time measuring large speeds (>5 cm s^{-1}), thus even time-averaged speeds that are small in amplitude (<1 cm s^{-1}) are significant.

Table 1. Mooring Location and Instrument Setup[a]

	Latitude	Longitude	Bottom Depth (m)	Instrument Depth (m) Additional Sensors	% Data Return
M1	65 19.6	112 56.1	1026	(T/P): 505, 1006 m	96, 99
M2	64 53.0	113 17.6	1517	(T/P): 496, 997 m	90, 0
				(T): 1497 m	81
M3	64 23.9	113 18.3	2518	(T/P): 501, 1000, 1996, 2498 m	78, 42, 0, 62
M4	63 15.7	113 19.8	3520	(T/P): 507,[b] 1006 m	100, 0
				(T): 2006, 3002, 3505 m	100, 97, 96
M5	61 50.3	113 17.2	4198	(T/P): 482, 980, 1980, 2980, 3675 m	0, 100, 100, 100, 100
				(T): 4178 m	100

[a]T and P indicate whether the VACMs included temperature and pressure sensors. Data return is provided for the velocity data only, as a percentage of the duration of the deployment (750 days).
[b]The VACM at this location provided no usable data and was replaced by the record at the bottom of the ADCP range at 460 m. Data return is provided for the ADCP record.

Additional data were obtained along the mooring line during the recovery cruise in January 2012 (Figure 1). Temperature and salinity measurements from a CTD (Seabird911) as well as direct velocity measurements from a Lowered ADCP (LADCP) were collected along the mooring line. These measurements were obtained at higher horizontal resolution (5–10 km) providing a useful tool to estimate length scales of the flow and

Table 2. Data Statistics[a]

			Mean (cm s^{-1})	STD (cm s^{-1})	τ_{int} (days)	τ_0 (days)	N_{eff}	Standard Error (cm s^{-1})
M1								
	505 m	u	−2.7	7.7	14.3	38.0	37	1.3
		v	0.3	4.4	3.6	4.3	146	0.4
	1006 m	u	−6.8	10.5	1.6	1.2	335	0.6
		v	0.8	3.9	3.6	4.4	147	0.3
M2								
	496 m	u	−1.1	3.8	5.8	3.8	91	0.4
		v	−0.5	3.9	1.0	1.0	512	0.2
	1497 m	u	−5.1	5.8	2.4	3.7	221	0.4
		v	−0.1	6.3	1.1	1.0	495	0.3
M3								
	501 m	u	−1.1	4.5	5.6	5.7	95	0.5
		v	−0.2	2.5	1.9	4.0	275	0.1
	1000 m	u	−1.6	3.2	11.1	8.0	32	0.6
		v	−0.3	1.8	1.8	4.0	201	0.1
	2498 m	u	−4.1	3.9	15.1	7.5	35	0.6
		v	−1.6	2.5	2.3	2.3	230	0.2
M4								
	460 m	u	1.1	5.1	9.7	10.4	55	0.7
		v	1.5	5.5	6.7	7.5	80	0.6
	2006 m	u	−1.4	4.6	10.2	11.2	52	0.6
		v	−0.4	4.9	6.8	7.2	78	0.6
	3002 m	u	−3.0	4.6	10.8	13.2	49	0.7
		v	−1.4	4.5	6.3	6.8	85	0.5
	3505 m	u	−3.7	5.0	9.9	13.2	54	0.7
		v	−1.8	4.5	5.7	6.7	93	0.5
M5								
	980 m	u	4.1	6.3	16.0	26.2	33	1.1
		v	−1.6	5.5	14.9	30.7	36	0.9
	1980 m	u	2.8	5.6	15.4	25.1	35	1.0
		v	−1.1	5.2	15.1	31.3	35	0.9
	2980 m	u	2.2	5.2	14.1	23.0	38	0.8
		v	−1.0	4.6	18.3	54.2	29	0.8
	3675 m	u	1.8	5.4	14.5	24.1	37	0.9
		v	−0.1	4.9	16.0	33.5	33	0.8
	4178 m	u	1.3	5.5	12.3	23.1	43	0.8
		v	0.0	5.1	15.3	14.2	35	0.9

[a]Mean, standard deviation (STD), decorrelation time scale (as integral time scale, τ_{int}, and as zero-crossing of the autocorrelation function, τ_0), number of degrees of freedom (N_{eff}), and standard error for the 17 month zonal, u, and meridional, v, velocity records.

assess the ability of the moored array to resolve the horizontal structure of the ASC (section 3.2.1). These data are also used to estimate the flow between the shallowest instruments at 500 m and the surface (section 3.2.2).

We also use surface geostrophic velocities produced by Ssalto/Duacs and distributed by Aviso (http://www.aviso.altimetry.fr/duacs/). These are provided at daily resolution and extracted at approximately 113°E from Aviso's 1/4° × 1/4° grid. These data are used to guide an estimate of the deep circulation in the region to the north of the moored array (section 3.2.3).

2.2. Current Meter Data Processing

The VACM data were processed following the standard procedure (Woods Hole Oceanographic Institution Technical Memorandum, WHOI-3-88). A number of additional adjustments followed the standard processing, mainly involving raw pressure data. Pressure drift was removed by applying linear, piecewise linear, and higher-order polynomials on a case-by-case basis. Synthetic pressures were generated for those instruments without pressure sensors by linearly interpolating the instruments above and below. Pressure transients due to mooring motion in the corrected time series did not exceed 10 db in any of the instruments at sites 1–3. At the deeper sites, the maximum pressure fluctuations recorded reached 80 db. All velocity and temperature records that experienced fluctuations in pressure exceeding 10 db were corrected for via linear interpolation. These corrections had minimal impact on the velocity data due to the very weak vertical shear recorded by the moorings.

To remove the effect of tidal and inertial frequencies all current meter records were low-pass filtered with a butterworth filter with a 2 day cutoff, run forward and backward, and subsampled at daily resolution.

3. Results

3.1. The Structure of the Flow

Temperature data collected during the recovery cruise (Figure 2) show the general structure of the density field across the array. Moorings 2–4 are located within the area where isopycnals slope upward toward the south below 500 m depth, corresponding to positive geostrophic shear (eastward velocities when integrated from the bottom upward). M1 is located at the latitude of the ASF, just below the 0°C surface isotherm during summertime conditions. At the ASF the slope of the isopycnals reverses, tilting downward to the south with no evidence of the V-shaped structure characteristic of dense water formation sites. However, time-mean velocity vectors (Figure 2) show that near-bottom velocities at moorings M1–M4 are westward, with a speed of 3.6 cm s^{-1} at M4 monotonically increasing to 6.8 cm s^{-1} at M1. The standard errors for these means (see Table 2) are 10–20%, indicative of a robust estimate of the near-bottom westward flow along the continental slope. Higher in the water column, zonal velocities are westward but weaker in magnitude, consistent with the weak positive shear implied by the southward shoaling of the isopycnals. The north-to-south gradient of the westward near-bottom flow is also

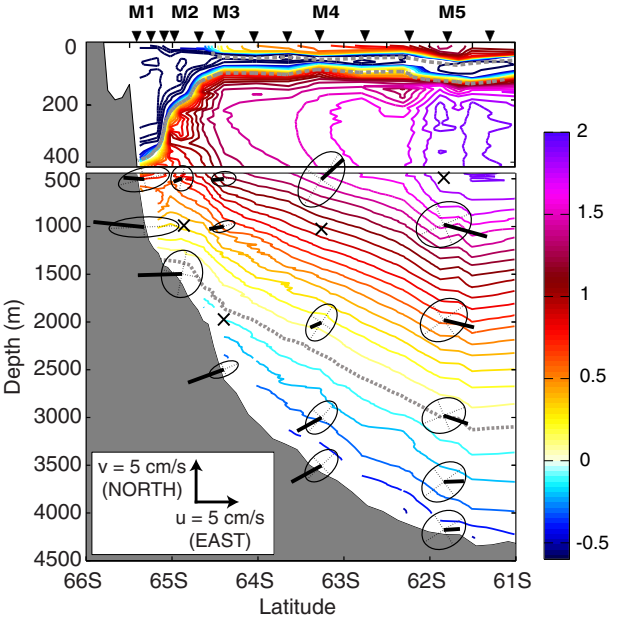

Figure 2. Variance ellipses and mean velocity vectors for each of the current meter records. The east and northward directions of both ellipses and mean velocity vectors correspond to right and upward, respectively, as indicated in the inset. Black crosses indicate instruments that recorded no data. The colored contours show full resolution potential temperature (in °C) from the recovery cruise. The black markers along the top axis indicate the position of the CTD stations. The 0°C isotherm is shown in by the dashed gray contour. The vertical axis on the top 500 m has been stretched.

consistent with the broad-scale deep density field: isopycnals steepen and near-bottom flow increases in the upslope direction.

Further offshore, the deep flow transitions from westward to eastward around the 4000 m isobath. The near-bottom instrument at M5 records a mean eastward flow 1.3 cm s^{-1} (with standard error of about 80%). The mean-velocity vectors in this region are in the direction of the geostrophic shear and consistent with the typical structure of the ACC domain with surface-intensified eastward flow. The placements of M4 and M5 were based on the regime boundary between bottom-intensified westward flow and surface-intensified eastward flow deduced by MD07 at I9S, and the moorings confirm this transition. The hydrographic properties at sites M4 and M5 are consistent with the properties of the Southern Boundary of the ACC (SB) and the southern branch of the SACCF (SACCF-s) south of Australia [*Sokolov and Rintoul*, 2002].

The zonal flow reversal described in MD07 reflected a cyclonic gyre in the southeastern Indian Ocean east of the Kerguelen Plateau. The array was placed across the eastern part of that gyre. Consistent with their inference, the current vectors at moorings M3–M5 show a southward flow toward Antarctica, a flow converging CDW toward the continent.

Time series of zonal and meridional velocities from the current meters (Figure 3) as well as variance ellipses (Figure 2) show the different character of the flow at different mooring sites. The variability, like the mean, is bottom-intensified at M1–M3 and is surface-intensified at sites M4 and M5. At sites M1, M3, and M4 the variability is more or less aligned with the direction of the mean flow (as indicated by the small angle between the mean velocity vectors and the major axis of the variance ellipses, Figure 2). At M2 and M5, ellipses are less elongated and the angle between their major axis and the mean flow is larger, indicating a more variable flow direction here.

On the upper slope the variability is dominated by higher-frequency oscillations with periods less than 1 week. At the bottom of sites M1 and M2 a signal with period 2–5 days dominates the record, more evident in the zonal component at M1 and the meridional component at M2. These frequencies have been linked to Coastally Trapped Waves at other locations around the Antarctic continental slope [*Jensen et al*., 2013; *Nakayama et al*., 2014]. Alternatively, energetic motions in this frequency band can also be explained by meso and submesoscale eddies formed at the ASF. Both eddies and coastal waves are likely to contribute to the cross-slope circulation. In this study we focus on the along-slope transport, for which the observed

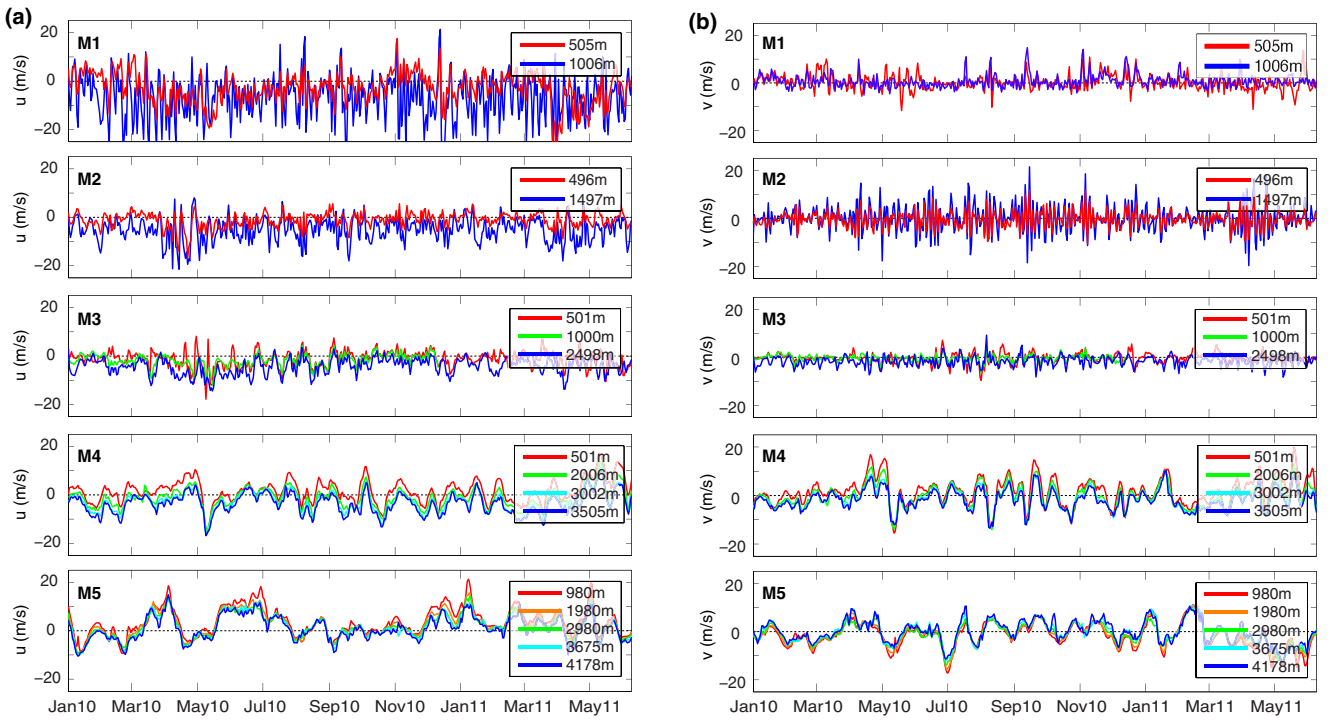

Figure 3. Time series of (a) low-pass filtered zonal and (b) meridional velocities (cm s^{-1}).

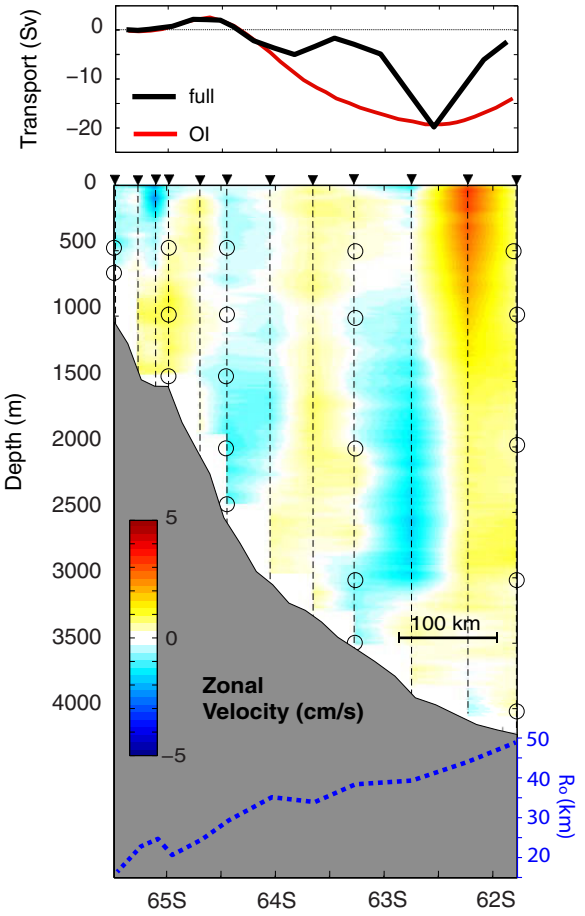

Figure 4. (Bottom) The color sections show LADCP zonal velocities collected during the recovery cruise at the locations indicated by the dashed lines. The open circles show the approximate location of the moored instruments at which the LADCP data are subsampled. In dashed blue along the bottom axis values for the first baroclinic radius of deformation (km) are shown as a function of position on the slope. (top) The black line shows the cumulative transport obtained from the full resolution data (full). In red is the transport from the subsampled data after it has been mapped back to full resolution via objective interpolation (OI).

2–5 day oscillations have no contribution. However, they are the dominant mode of variability at sites M1 and M2, and in order to explore other modes of variability and their contribution to the ASC transport, in section 3.2.1 we calculate Empirical Orthogonal Functions (EOF) from the low-pass filtered records with a 7 day cutoff.

On the lower slope, the spectrum of both components of the velocity at M4 and M5 is red with distinct peaks at the diurnal and semidiurnal periods (not shown), and energy is concentrated around the typical decorrelation time scales for the flow at M4 and M5 (15–30 days and Table 2), suggestive of open ocean eddy processes.

Velocities are very coherent in the vertical direction, more so in the deeper moorings, where there is little energy at shorter periods. Across mooring sites, the coherence between records is minimal, even on the upper slope where instruments are only 50 km apart.

3.2. The Transport of the ASC

In this section we estimate the total transport of the ASC across 113°E. The moored array spans the water column from 500 m to the seafloor south of 62°S. Integration of the velocity field gives the transport across the array, which makes the dominant contribution to the total transport. To get the total transport, we then estimate the transport in the upper 500 m south of 62°S by integrating geostrophic velocities from the recovery cruise. These upper 500 m are not directly measured by the moored array. Finally, we estimate the top-to-bottom transport north of 62°S from a satellite-based reconstruction of the velocity field; this component is large at times when the westward flow extends beyond the array limits.

3.2.1. Transport Through the Moored Array

The main challenge in estimating transports from this data set is the large spacing between moorings. The spacing was a trade-off between measuring far enough to reach the eastward limb of the hypothesized gyre and properly resolving the circulation inside the westward flow. As a result, the moorings were separated, from south to north, by 52, 54, 126, and 158 km, respectively. The lack of coherence between mooring sites seen in the velocity time series suggests that the typical lateral scales of the time-varying currents are smaller than the spacing between moorings. LADCP zonal velocities from the recovery cruise (Figure 4) suggest that the width of the bands of positive/negative flow ranges from 50 to 100 km. Although it is uncertain how typical this velocity snapshot is, the location and vertical structure of some of the main features in the circulation measured by the moorings are well captured by the LADCP: surface-intensified westward flow at mooring site M1, bottom-intensified westward flow in the vicinity of sites M3 and M4, and strong surface-intensified eastward flow near site M5.

To determine the sensitivity of the transport estimates to the distance between moorings, we first subsample the LADCP data at the mooring locations, objectively map them back to the original resolution,

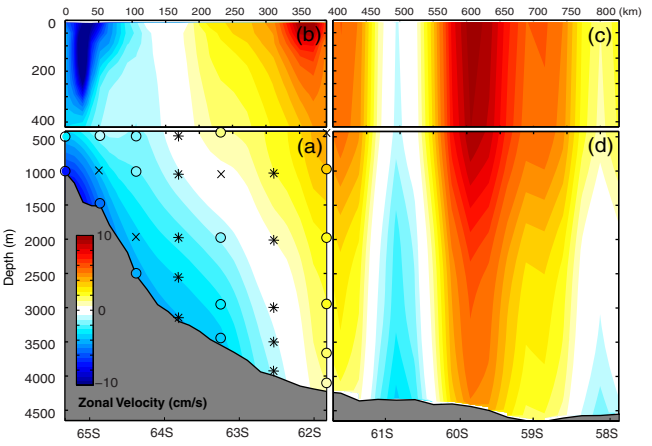

Figure 5. Mean zonal velocity sections (in cm s^{-1}). Figure 5a shows the Eulerian mean of the gridded zonal velocity from the moored array. Colored circles show the time-mean velocity for each of the VACM records. Black crosses indicate the location of failed records that are filled by linear interpolation, and stars indicate the position of the synthetic mooring records (see section 3.2.1). Figure 5b shows the absolute velocity in the top layer obtained from referencing geostrophic shear from the recovery cruise to moored velocity at 500 m (see section 3.2.2 for details). The vertical axes have been stretched. Figures 5c and 5d show the time-mean zonal velocity obtained by reconstructing the vertical structure of the flow from altimetry (section 3.2.3). The vertical axis in Figure 5c has been stretched for consistency.

excluding the top 500 m the moorings did not sample, and compare the effect of the reduced resolution and the mapping on the integrated transports. Our results are not sensitive to the vertical scale, since the moorings are more coherent in the vertical. Subsampling the LADCP velocities at the mooring locations has a large impact on the structure of the flow and a moderate effect on the transport, up to 20% of the maximum transport depending on the mapping scales (Figure 4).

The first baroclinic Rossby radius of deformation, R_o, can provide another scale for the flow [*Thompson et al.*, 2014]. We estimate R_o as NHf^{-1}, where N is the buoyancy frequency calculated from the hydrographic observations, H is the water column depth, and f the Coriolis frequency. Values range from 20 km in the upper slope to 50 km at the deep end of the array (Figure 4). These scales are comparable to the LADCP station spacing. Hence even at the southern end of the array, where observations are closer together, we may not fully resolve the velocity structure.

To quantify the effect of small-scale structure in the transport, we performed a series of tests using synthetic jets. Details of these experiments are provided in Appendix A. Our findings suggest that 50 km regularly spaced observations, regardless of jet width, are sufficient to resolve the time-mean transport within 2% of its value. However, errors can be as large as 10% when observations are irregularly spaced over distances ranging from 50 to 150 km. Accurately resolving variability is more sensitive to the width of the jets and the spacing between observations. Only when the width of the jets equals or exceeds the spacing between observations, we can accurately resolve the variability.

In the remainder of the paper mean and time-varying zonal velocities and transports are obtained by objectively mapping the current meter records. Gaps in the vertical due to instrument failure are filled in by linear interpolation of the instruments above and below. In addition, at the midpoint between mooring sites M3–M4 and M4–M5, where the gap between the moorings is larger than the horizontal decorrelation scales, prior to mapping we create synthetic mooring profiles by linearly interpolating the records at either side. This allows us to maintain a small decorrelation scale in the mapping consistent with the observations (50 km), while preventing the interpolation from creating values outside the range measured by the deep moorings. Time-mean transports estimated this way are not sensitive to the horizontal mapping scales. However, small-scale velocity structure shorter than the real profile spacing remains unresolved by this approach.

The Eulerian mean section of the 17 month objectively mapped zonal velocities (Figure 5a) shows bottom-intensified westward flow along the sloping bottom, inshore of the 2000 m isobath. This westward flow progressively weakens offshore out to M4. The flow transitions to eastward in the upper layers near the 3000 m isobath, and at depth offshore of the 4000 m isobath. The maximum cumulative westward transport through the region covered by the moored array (south of 62°S and below 500 m) reaches a maximum value of −12.2 Sv near 62.5°S, where the deep flow transitions to eastward.

Because the current axis moves, the transport due to the mean flow averaged over a fixed latitude band does not represent the mean transport of the synoptic flow. To account for changes in the axis of the ASC over time, we integrate the zonal velocity out to the maximum in cumulative westward transport at every

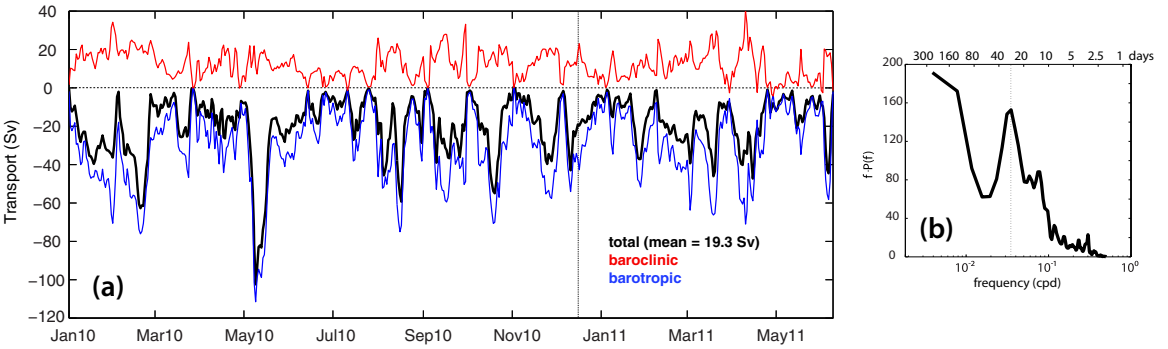

Figure 6. (a) Time series of maximum cumulative westward transport for the array cross section between 500 m and the bottom (in Sv). In black is the total, in blue the barotropic component, calculated as bottom velocity times water depth (excluding the top 500 m), and in red the baroclinic component, as the difference. The vertical line indicates the time when the VACM at 1000 m in M3 fails, and the record is extended by vertical interpolation between adjacent instruments. (b) Energy conserving spectrum of the total transport (black line in Figure 6a).

time step. The resulting time series (black line in Figure 6a) shows a highly variable flow, with transports ranging from 0 to −100 Sv, fluctuating over periods of 25–30 days (Figure 6b). Averaged over the 17 month period, we estimate a mean westward transport through the array below 500 m of -19.3 ± 1.9 Sv. The standard error is calculated based on the decorrelation time scale of the transport time series (8.5 days).

Two additional lines are shown in Figure 6. In red, we show the transport calculated by referencing the zonal velocity to 0 at the bottom, that is the baroclinic component, and in blue is the barotropic component calculated as the bottom velocity times the water depth (excluding the top 500 m). The latter is large and negative and dominates the total transport. The contribution from the baroclinic shear slightly reduces the transport.

The time-varying flow often changes sign in the upper part of the water column at M4 and occasionally at other moorings. For this reason, the sum of just the westward flow across the array yields slightly larger transports (−21.2 Sv) than the maximum cumulative westward transport.

Fluctuations in the transport can be several times larger than the mean. In order to characterize this variability and determine how the different elements of the circulation across the array contribute to the transport, next we calculate Empirical Orthogonal Functions (EOF) of the zonal velocity. We focus here on the three leading EOFs which explain, respectively, 55, 28, and 7% of the variance in the data (Figure 7).

The leading mode, EOF1, consists of a single-signed more or less vertical uniform velocity anomaly concentrated at the offshore end of the array, with velocities in excess of 5 cm s^{-1} in the top 2000 m at M5. To quantify the contribution to the transport by the modes, we add and subtract the mode times 1 standard deviation to the mean zonal velocity, then integrate vertically and meridionally (Figure 8). At the location of the transport maxima EOF1 is responsible for fluctuations in the transport of −12.9 Sv (larger when PC > 1), equivalent to 55% of the transport variability. When the mode is negative (PC < 0, eastward velocity anomaly), the maximum cumulative transport is reduced to less than −5 Sv and limited to the southern end of the array, inshore of the 3000 m isobath; offshore the flow reverses sign and flows eastward. When the mode is positive (PC > 0, westward velocity anomaly) the westward flow offshore of the 3000 m isobath is intensified and the location of the maximum transport shifted northward. This pattern of alternating positive and negative velocity anomalies at M5 is also seen in the altimeter record (Figure 9), as eastward or westward flowing jets that develop over periods of a few months and propagate northward. Jet migration is a common feature in geophysical flows that occurs when there is a gradient in the background potential vorticity (PV). Here like in *Stern et al.* [2015], the PV gradient is generated by the slopping bottom. However, the width of the migrating jet is likely overestimated by the mode, as the signature of a narrow jet propagating across moorings separated by more than one jet's width is aliased across mooring sites in the EOF (see Appendix A).

In terms of transport, the overall result of these propagating jets is a change in the extent of the ASC, the latitude where the transport transitions from westward to eastward. And in fact, PC1 is well correlated with the latitude at which the maximum westward transport occurs in our transport time series.

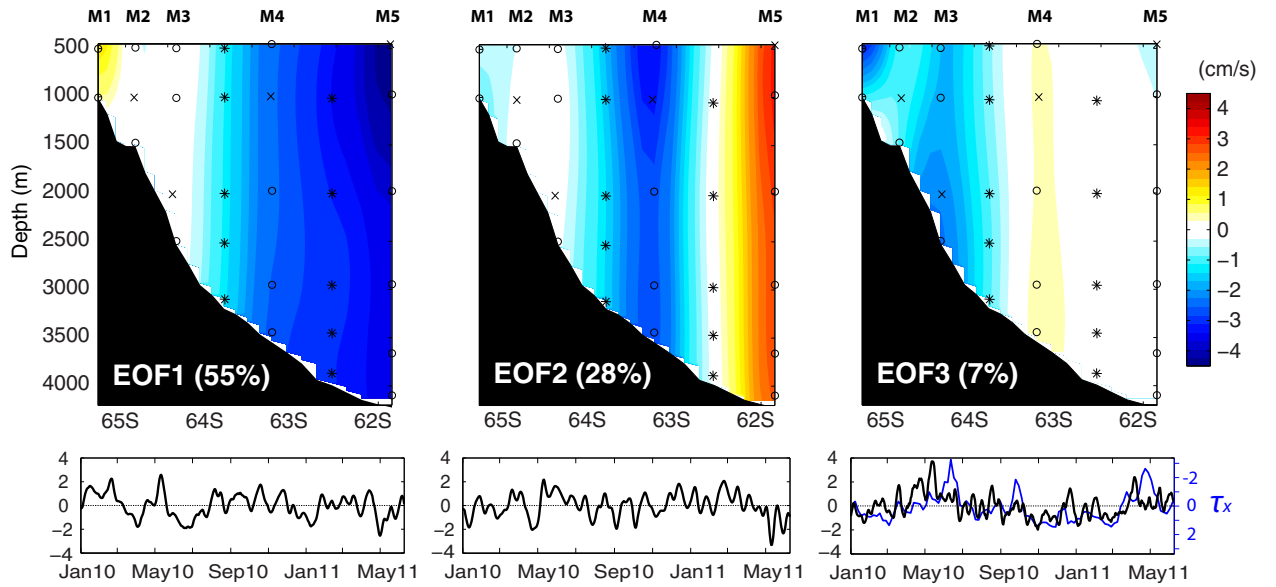

Figure 7. Leading EOFs of the zonal velocity. Color sections on top show the spatial pattern of the three leading modes, and the corresponding fraction of the variance explained. The modes are scaled to display cm s^{-1}. Black circles, crosses, and stars indicate the location of full records, failed instruments, and synthetic records as in Figure 5. On the bottom, the standardized principal component (temporal pattern) associated with each mode. Superimposed on mode's three principal components in blue is the standardized zonal wind stress, τ_x, at 115°E and 65°S obtained from NCEP reanalysis [*Kalnay et al.*, 1996].

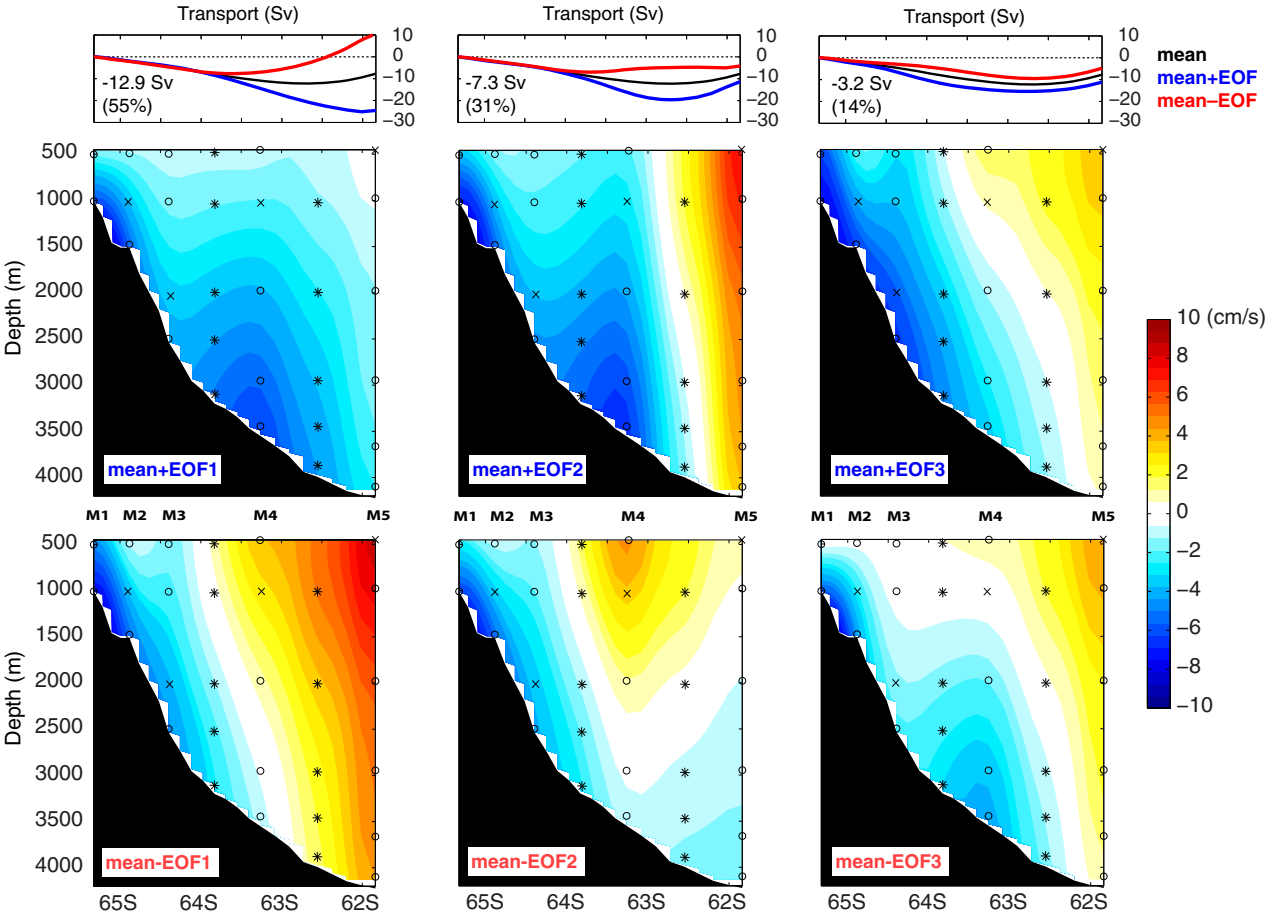

Figure 8. The color sections show the mean zonal velocity plus (center) and minus (bottom) the three leading EOFs. Black circles, crosses, and stars indicate the location of full records, failed instruments, and synthetic records as in Figure 5. The top show in blue and red the transport associated with the combined mean plus or minus EOF. The transport by the mean is shown for completeness in black.

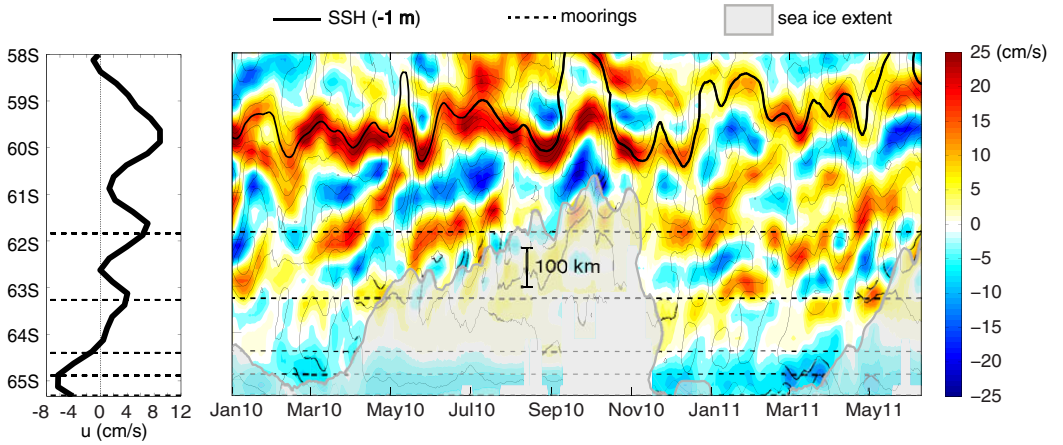

Figure 9. Zonal geostrophic velocities (cm s^{-1}) derived from the altimeter at 113°E. (left) Time-mean velocities for the 17 month period. The latitude of the moorings is shown by the dashed lines. (right) Time-varying velocities. Superimposed are SSH contours in black, with the thick line showing the −1 m contour corresponding to the SACCF-n. Sea ice extent (from the National Snow and Ice Data Center) is shown by the gray shaded area.

EOF2 also captures nearly vertically uniform fluctuations at the deeper end of the array, but now with two separate cores, centered at M4 and M5, of different sign. The transport fluctuations associated with these features are on the order of −7.3 Sv (28% of the transport variability), amplifying the magnitude of the transport maximum when in the negative phase, and reducing and slightly shifting the transport maximum when in the positive phase. The spatial pattern of this mode resembles the structure of a ring. Cyclonic eddies are well documented in the continental slope at this longitude [*Wakatsuchi et al*., 1994], as well as further to the east [*Aoki et al*., 2007]. Although the flow structure of EOF2 is consistent with the flow pattern of the reported eddies, the scale is larger than the typical size of the eddies, 80–150 km according to *Aoki et al*. [2007]. The signature of a propagating jet aliased into the observations can also appear in higher modes as two separate anomalies with opposite sign. However, the lack of correlation between PC1 and PC2 indicate that these modes represent different sources of variability (Appendix A), possibly related to the occurrence of single versus multiple jets across the array.

EOF3, in contrast to the previous modes, consists of two baroclinic velocity cores: one is bottom-intensified and centered at M3, and the other is surface-intensified and located at M1. The mode's contribution to the transport is on the order of −3.2 Sv (14% of the transport variability), smaller than EOF1 as the flow on the upper slope is much more steady in time and the mode's signature is confined to shallower water. The principal component associated with this mode is the only one that exhibits seasonality. Averaged over the winter months (April–September) PC3 is −0.5, and is 0.5 during the summer months (October–March), corresponding to approximately 2 Sv fluctuations in transport. However, when the westward flow reaches its maximum in April–May, the mode's contribution to the transport can be up to 15 Sv. The timing of the seasonal cycle in EOF3 is in good agreement with the annual cycle of the wind, as shown by the zonal wind stress at the location of the array (Figure 7). We discuss this possible connection with wind forcing in more detail in section 4.

3.2.2. Transport in the Upper 500 m: Contribution From the ASF

Constrained by the need to remain clear of passing icebergs, the upper 500 m of the water column were not sampled by the array, with the exception of the ADCP located at site M4 that profiled currents acoustically upward from 500 m. Data collected by this instrument are not used to resolve the transport in this upper layer, as the instrument was located at the transition between the westward and the eastward flow within the upper water column, where velocities are particularly weak and there is little coherence in the horizontal between adjacent moorings. However, velocities measured by the ADCP are in very good agreement with those we estimate next, validating our approach.

To reconstruct the flow in the upper 500 m of the water column, we make use of the fact that the flow is much more baroclinic within the ASF than further offshore. Geostrophic shear calculated from the density field from the recovery cruise (Figure 10) shows baroclinic velocities are concentrated in the upper 500 m.

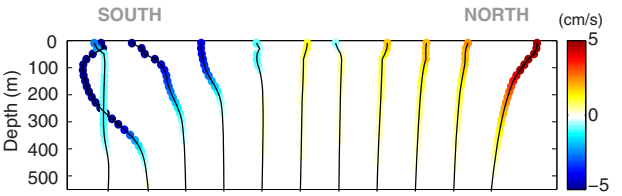

Figure 10. Cross-track geostrophic velocity profiles (in cm s^{-1}) in the top 500 m between 65.5 and 62°S calculated from the recovery cruise. The profiles have been referenced to 0 at 500 m and shifted from south (left) to north (right) to better show their structure.

Referenced to zero at 500 m, these velocities tend to be large and positive (>6 cm s^{-1}) on the northern end of the array, and large and negative (<−10 cm s^{-1}) on the southern end, south of 64.5°S.

Rather than referencing these relative velocities to the cruise shipboard ADCP (SADCP) or LADCP, which are noisier and only representative of summertime conditions, we reference the geostrophic shear to the time-varying velocities at 500 m from the moored array, averaged every 14 days to eliminate the contribution from waves and other non-balanced motions. Before referencing the data, geostrophic velocities are mapped on to the same grid as the current meter data. The maximum westward transport from the gridded geostrophic shear relative to 500 m is −1 Sv. The transport by the absolute velocity in the ASF ranges from −0.6 to −7.6 Sv, with a mean value of −2.3 Sv, double the baroclinic component.

The maximum surface velocity in the time-mean absolute velocity field resulting from the referenced geostrophic velocities (Figure 5b) is −10 cm s^{-1} and located at approximately 65°S in water depths of 2000 m. North of the ASF, the surface velocity is eastward. At M4 the eastward flow is weaker, and restricted to the upper 1000 m. Further north, at 62°S, the eastward flow intensifies and reaches all the way to the bottom. In the altimeter this broad eastward flow is separated into two jets, a weak one centered at M4 and a stronger one centered at M5. Both these jets form somewhere along the continental slope at depths greater than 3000 m and propagate northward where their signature disappears (Figure 9). The mean location of these jets corresponds to the fronts previously identified as the SB and SACCF-s at M4 and M5, respectively.

3.2.3. Transport North of 62°S

Westward transport derived from the objectively mapped velocities within the array reach their maximum value at the northern end of the array (at M5) 27% of the time (Figure 11, bottom). These times correspond to high ASC transport events: the mean transport resulting from averaging only this 27% of the record is −31 Sv, compared to the −15 Sv obtained when the same 27% of the record is excluded. During these times, the actual northern boundary of the westward flow is likely to be north of M5, and thus the ASC extends beyond the array. In this section, we use satellite altimetry to estimate the transport due to the flow north of M5.

North of M5 the altimeter record is relatively unaffected by ice and can provide surface geostrophic velocities. However, in order to reconstruct the full three-dimensional velocity north of the moored array, we also need information about the vertical structure of the flow. Typically, this is done in the ACC by assuming the barotropic component of the flow is small and the full vertical structure is well represented by the steric or baroclinic component alone [e.g., *Sun and Watts*, 2001]. However, at M5 the variability is predominantly barotropic, it has a large near-bottom component and is nearly vertically uniform, as seen in the leading EOF calculated from the zonal velocity at M5 alone (Figure 12). This mode captures over 97% of the variance at the site, and has values of 5.7 cm s^{-1} at 1000 m and 4.6 cm s^{-1} at the bottom, just a 1.1 cm s^{-1} change in magnitude over a 3000 m depth change. This barotropic variability is not properly represented by methods that rely on the steric component alone. So rather than decomposing the flow into a baroclinic and a barotropic component, our approach is to use the leading EOF of the zonal velocity at M5 to construct a velocity profile associated with each surface geostrophic velocity value from the altimeter data. The method is the following. First the zonal velocity from M5 is vertically extrapolated to the surface using constant shear from the instruments below. Next, the EOF mode and the mean are vertically stretched to match the local depth, which increases by 500 m to the north. The mean profile is then added back to the variability. And finally mode plus mean are scaled to span the range of surface velocities observed in the altimeter north of M5, producing a single velocity profile for each surface velocity value. This approach assumes that the shear is linear within the top 2000 m and the flow north of M5 has the same vertical structure we observe at M5. Geostrophic shear north of 62°S from various repeats of the I9 line suggests that, to the leading order, these assumptions are valid south of the northern branch of the southern ACC front (SACCF-n), typically found at 60°S.

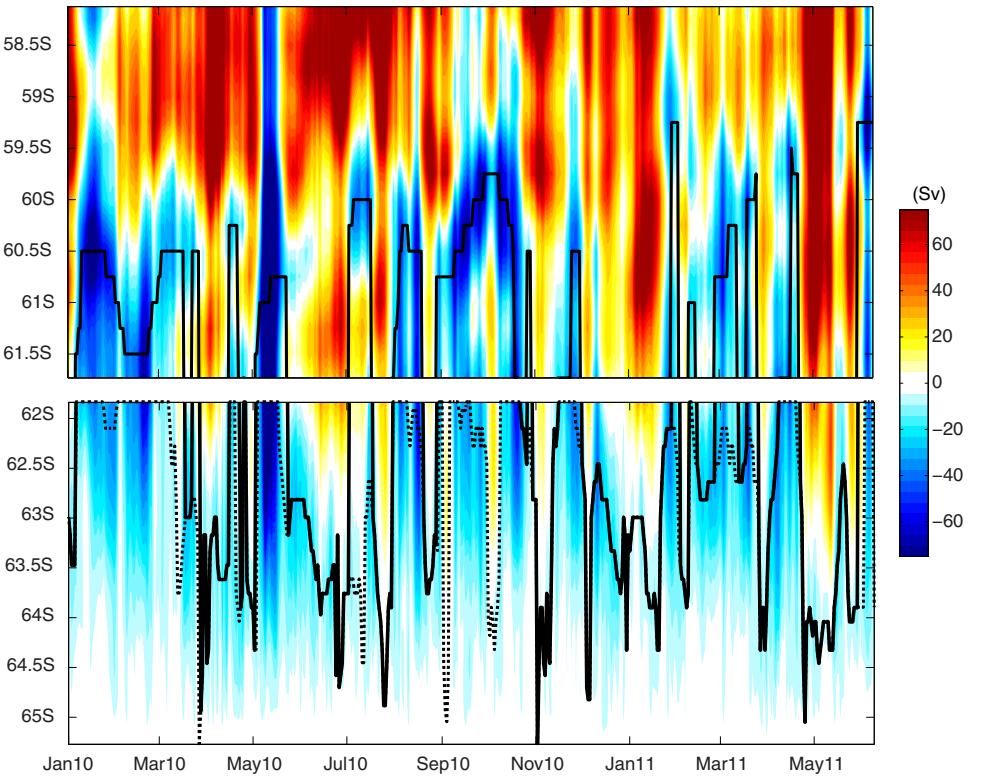

Figure 11. Time series of cumulative transport (in Sv) versus latitude. Positive transports are eastward. The bottom figure shows the transports obtained from the objectively mapped zonal velocity from the moorings. The top figure shows the extended transport derived from the reconstructed zonal velocity field from the altimeter. In the bottom figure, the dashed black line shows the location of the maximum westward transport from the mooring data alone. The thick line shows the latitude of the maximum westward transport when the satellite extension is included.

The time-mean zonal velocity that results from applying the extrapolation for the entire mooring period between 62°S and 58°S is shown in Figures 5c and 5d. The northern flank of the eastward jet captured by the M5 mooring extends to 61°S. Further north, a narrowband of bottom-intensified westward flow separates the eastward jet at 62°S from a stronger eastward jet with velocities exceeding 5 cm s^{-1} at the bottom. The core of this strong jet is located approximately at 60°S. Temperature and salinity data collected during the recovery cruise indicate it is the SACCF-n.

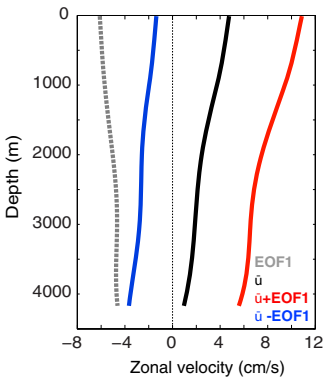

Figure 12. Leading EOF of the zonal velocity from M5 alone in dashed gray. This leading mode captures over 97% of the variability at M5. The mean velocity profile at M5, linearly extrapolated to the surface, is shown in black. The red and blue lines show the mean plus and minus the EOF (times 1 standard deviation).

The time-varying cumulative westward transport that is associated with the flow north of 62°S can now be obtained by integrating northward from the deepest mooring out to the extended velocity field. At times, the cumulative transport maximum is found as far north as 60°S (Figure 11, top), in water depths of 4500 m. However, when the maximum is at these northern latitudes the westward transport across the deeper end of the moored array is sometimes blocked by eastward flow, and the westward flow appears to be diverted further offshore.

The additional transport through this extended flow from the surface to the bottom varies from 0 to nearly 40 Sv at some localized events (Figure 13). Averaged over the 17 month record it contributes an additional −7.6 Sv to the mean. While this method of extrapolation can underestimate the shear in the top 500 m, as the flow becomes more baroclinic to the north, it is also likely that the method overestimates the flow at depth, partially compensating the reduced shear in the upper part of the water column.

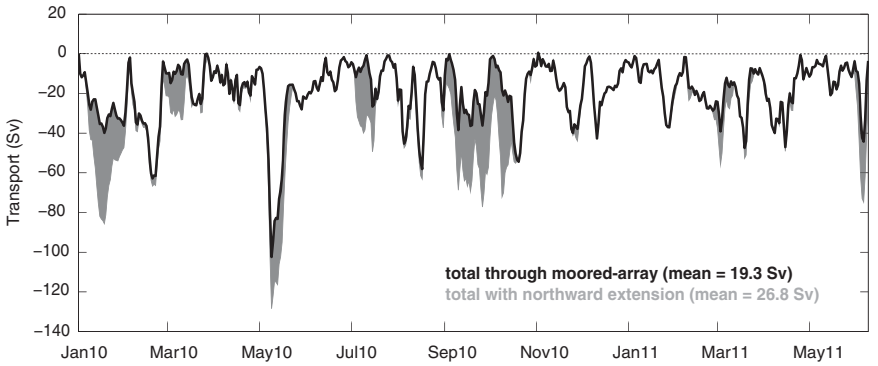

Figure 13. In black is the time series of maximum westward transport through the moored-array domain (below 500 m as in Figure 6). The gray shaded area shows the additional full depth westward transport associated with the northward extension of the flow.

4. Discussion

We have estimated three elements contributing to the total transport of the ASC: the moored array (below 500 m), −19.3 Sv, the upper 500 m above the array, −2.3 Sv, and the area immediately to the north of the array, −7.6 Sv. Thus, the estimated total time average transport of the ASC is −29.2 Sv. This is less than half the estimate of −76 Sv from the MD07 analysis from the I8S and I9S sections. We now discuss the ASC transport in the broader context of Southern Ocean circulation estimates and follow with some thoughts about the causes of the strong ASC synoptic variability.

4.1. The Mean: Previous Estimates

Long-term direct velocity observations over the continental slope of East Antarctica are very limited. *Bindoff et al*. [2000] characterized the circulation over the slope between 80 and 150°E based on a combination of synoptic observations, including surface drifters, SADCP, and geostrophy. Across the region, the average surface drifter velocity they observed is −16 cm s^{-1}, in water depths of approximately 500 m. The maximum surface velocities they obtain from the SADCP for the westward flow above the upper slope range from −16 to −18 cm s^{-1} across the various sections. Although not directly sampled by our array, the reconstructed maximum surface velocity we obtain is −10 cm s^{-1}, and is found where water depths are between 1000 and 2000 m.

Direct velocity measurements from a 13 month record at 140°E have shown bottom-intensified flow, with values along the 2600 m isobath of −16 cm s^{-1} at the bottom, and −5 cm s^{-1} at 1075 m [*Fukamachi et al*., 2000]. At our site, record mean speeds along the 2500 m isobath are several times smaller (−4 cm s^{-1} at the bottom and −2 cm s^{-1} at 1000 m). Lower velocities at our site may be due to the lack of dense water formation in the area, as Fukamachi's observations were located along the path of the descending bottom water from the Adelie Land-Mertz Glacier region. *Bindoff et al*. [2000] also noted that much stronger bottom flows tend to occur in areas where they found evidence of dense water formation. MD07's SADCP-referenced I9S section at this longitude extended as far south as the 2655 m isobath (shallower sampling was precluded by ice conditions). Their bottom velocities for the ASC ranged from 0 to 7 cm s^{-1}.

Integrated from the southern end northward, *Bindoff et al*.'s [2000] ADCP-referenced geostrophic calculation yields a transport of −29.4 Sv averaged across all sections. This value is remarkably similar to ours, although the agreement is likely to be fortuitous, as their estimate excludes the northern part of our section and is an average of eight sections with transports ranging from −10 to −55 Sv. However, the averaging over several sections may eliminate some of the synoptic variability in Bindoff's estimate and reduce some of the errors associated with SADCP referencing, in part explaining the similarity between the two values. The MD07 SADCP-referenced I9S section had an ASC transport of −33 Sv at its southern end at the 2655 m isobath, roughly the site of our mooring M3. In our analysis the ASC carries −23.3 Sv to the north of M3.

Further to the west, the ASC has to supply both the flow through the Princess Elizabeth Trough (PET) and the Kerguelen Plateau. From a 2 year current meter record *Fukamachi et al*. [2010] estimated the time-mean deep western boundary current east of the Kerguelen Plateau carries 12.3 Sv of AABW northwestward. Using the temperature data collected during the recovery cruise to define the upper boundary of the AABW

(potential temperature less than 0°C), we find a transport of −7.4 Sv of AABW by the time-mean ASC. However, of these 7.4 Sv only part may recirculate north to supply the deep western boundary current off the Kerguelen Plateau. In the Weddell Sea *Thompson and Heywood* [2008] argued that only the deepest of three cores that form the ASC on the western side of the basin recirculates north into the gyre as the Weddell Front. The deepest westward flow in our section is found at M4. In situ temperatures at the bottom instrument in M4 are colder than −0.25°C year-round, sufficiently low to supply the core of the Kerguelen western boundary current. Some of the transport of AABW inshore of M4 may continue on to the PET, where *Heywood et al*. [1999] estimated a westward transport of water with potential temperature less than 0°C of −20 Sv, −45 Sv when integrated top-to-bottom. This latter value is within the observed total transport variability at our site.

However, some of the discrepancies between our and previous estimates could also be due to the uncertainties in our calculation. The first source of uncertainty is the limited spatial resolution of the data. Our analysis suggests that errors associate with small-scale velocity structure not resolved by the array are likely to remain less than 10% of the true time-mean value.

The second largest source of uncertainty comes from the lack of data in the upper 500 m where the ASF flow is the strongest. Our calculation of the ASF transport resolves changes in the barotropic flow of the ASF, through the referencing to the time-varying velocity from the moorings. However, it does not allow for changes in the baroclinic structure of the front. The work of *Moffat and Lentz* [2012] suggests that under enhanced downwelling favorable winds (westward for the Antarctic slope), buoyant plumes coming off the shelf become deeper and narrower, and the baroclinic structure of the front changes. Our CTD section is only representative of summertime conditions when winds are weaker. Changes to the vertical structure of the ASF during wintertime could lead to larger transports.

And last, our southernmost geostrophic velocity profile is south of 65.5°S, offshore of the 1000 m isobath, and additional flow could exist in shallower water. In particular, given the narrow shelf in this location, the Antarctic Coastal Current that is typically found on the shelf could merge with the ASF [*Heywood et al*., 1998]. *Thompson and Heywood* [2008] estimate the transport associated with the coastal current on the western side of the Weddell to contribute an additional 1.3 Sv.

4.2. The Variability: Wind Versus Dense Water Export

Our 17 month record shows a distinct seasonal cycle over the upper continental slope. Its signature is most evident at the top of M1 and near the bottom at M3. Although both wind and dense water formation could explain these seasonal changes, we believe it is wind rather than dense water formation that is responsible for the changes we observed in the upper layers and in the deeper flow at M3. Next we discuss some evidence from the literature in support of this argument.

The seasonal signal at the top of M1 can be explained by enhanced winds deepening and strengthening the ASF as described by *Moffat and Lentz* [2012]. Reanalysis wind stress over the continental slope (Figure 7) is maximum during the late autumn early winter period, when the velocity at the top of M1 reaches its maximum value. Temperature data from the top current meter at M1 further support this hypothesis. Unfortunately, the temperature sensor at this site stopped recording when temperatures dropped below 0°C. Nevertheless, the available temperature data (not shown) suggest that periods when temperatures are below 0°C, and the ASF is deeper, coincide with the strongest zonal velocities in the record. Other modeling [*Mathiot et al*., 2011] and observational [*Wåhlin et al*., 2013] studies have also shown that wind regulates the seasonal cycle of the ASF.

As to why the flow below the ASF is bottom-intensified, *Gill* [1973] first proposed that in areas where dense water is formed, plumes descending along the continental slope adjust geostrophically, and a bottom-intensified current develops along isobaths. This link between dense water formation and the strength of the ASC has been observed at other locations. For example, current meter observations on the continental slope at 140°E downstream of the dense water outflow from the Mertz polynya region show velocities that are several times larger near the bottom than those recorded at higher levels [*Fukamachi et al*., 2000]. The magnitude of these bottom flows, when close enough to the formation site, is correlated with temperature such that cold events are associated with larger than average speeds [*Williams et al*., 2010]. Although we also observe bottom-intensified flows in our data, the connection to dense water formation is not clear. The

increase in shear in the bottom instruments is much less than observed in areas of active dense water formation. In addition, bottom temperature data from our moorings, available at mooring sites 2 and 4, do not show any correlation with flow speed. This is also consistent with *Bindoff et al*. [2000], who found no evidence of dense water formation at their closest occupation to our mooring site (113°E).

The temperature sensors at the bottom of M1 and M3 did not record any usable data during the experiment. However, the bottom temperature records from M4 show slowly varying temperatures well below 0°C, suggesting dense water is present in the array, but in a more diluted form possibly originating at a remote location. This could explain the lack of correlation between cold events and enhanced velocity. Is then enhanced shear near the bottom indicating the presence of dense water from a distant source? This is the case in the Weddell Sea, where *Thompson and Heywood* [2008] find that the deepest of three observed fronts that contribute to the ASC is characterized by strong tilt in the isopycnals near the bottom. The authors link this enhanced shear at the bottom to the presence of dense water outflow originating upstream in the gyre. This is likely to be the case at M4, where the coldest water in the array is found.

On the upper slope, enhanced shear near the bottom can also be related to the dynamics of the bottom boundary layer. Ekman transport associated with the along-slope current is directed to the right in the Southern Hemisphere, downslope for the westward flowing ASC. This downslope flow moves lighter water downward increasing the tilt of the isopycnals near the bottom. However, the geostrophically balanced flow induced by the change in isopycnal tilt near the bottom should act to reduce or even reverse the interior westward flow near the bottom, a phenomenon that is known as Ekman arrest [*MacCready and Rhines*, 1991; *Garrett et al*., 1993]. Instead, the variability in EOF3 is bottom-intensified near M3. Nevertheless, the similar phase of the seasonal cycle at the top of M1 and the bottom of M3, as captured by EOF3, and the local zonal wind stress suggests that boundary layer dynamics driven by the wind may still be the responsible mechanism.

In deeper water, the variability of the westward transport is dominated by the blocking effect of the eastward jets at M4 and M5. The hydrographic properties of these jets are consistent with the properties of the SB and SACCF-s. When they move northward, the width of the ASC increases, and so does its transport. The northward migration of jets over the Antarctic continental slope can result from changes in the background potential vorticity gradient caused by the sloping bottom [*Stern et al*., 2015]. Stern's modeling work shows that over sufficiently wide slopes multiple jets can form, become baroclinically unstable, and migrate northward. This mechanism may be at play at our site and explain some of the variability we observe in the deeper moorings.

5. Conclusions

We used direct velocity moored observations off the continental shelf in East Antarctica, thermal-wind shear, and satellite-derived velocities to evaluate the mean structure and transport of the ASC and characterize its variability. The overall structure of the ASC is consistent with inferences from previous studies. The mean flow is bottom-intensified and directed westward inshore of the 4000 m isobath, and eastward offshore in deeper water.

We estimated the mean transport of the ASC to be −29.2 Sv, which consists of:

1. -19.3 ± 1.9 Sv between 500 m and the bottom south of 62°S, as directly measured by the moored array. This transport results from a large westward barotropic component, plus a small positive (eastward) baroclinic component.
2. −2.3 Sv carried by the flow within the ASF in the upper 500 m, where the flow was inferred from summertime measurements of geostrophic shear referenced to the mooring velocities. In contrast with deeper water, approximately half of this transport (1 Sv) is carried by the baroclinic component.
3. −7.6 Sv north of 62°S, at times when the transition from west to eastward flow occurs beyond the northern limit of the array. These northward extensions of the ASC occur 27% of the time, and their surface expression is captured by the altimeter record.

Fluctuations in the transport are several times larger than the mean. Changes in the flow in waters deeper than 3000 m account for more than 80% of the variability in the transport. These are in the form of jets, rings/meanders that develop in the lower slope and move through the array blocking the westward flow

and effectively changing the latitude of the boundary between the eastward and westward flow for periods ranging from several weeks to months. The flow in the upper slope is much more steady. Fluctuations there, account for the remaining 20% of the variability in the transport, and are dominated by the seasonal cycle, with maximum velocities during the autumn (April–May–June), when the wind stress is also maximum.

This large variability we observe implies that snapshots of the flow can lead to transport values that under or overestimate the time-mean to a large degree. This along with the predominantly barotropic nature of the flow, mean that long-term direct-velocity measurements like these are essential in order to monitor the mean circulation and changes in the continental slope around Antarctica, as well as supply valuable information to evaluate models.

Appendix A: Synthetic Jet Error Estimates

To quantify the error associated with small-scale structure across the array, we created a series of synthetic jets, with widths ranging from 10 to 100 km, spanning a distance of 400 km over a linear slope with 500 m at the southern end and 4500 m at the northern end. The jets are vertically uniform and have peak velocities at their cores of approximately 6 cm s^{-1}, chosen to match the vertically averaged velocities from the LADCP. The jets can propagate offshore across the section with a speed of 13 km per day so that a jet originating at the shallow end of the section travels through the domain in approximately 30 days (the decorrelation time of the deeper moorings). Then we add random noise to the jets' velocity and run the experiment for 100 days, to allow multiple jets to travel through the entire the domain. The section is then subsampled, first with a regular spacing of 50 km, and then with irregular spacings increasing from 50 km at the shallow end to 150 km at the deep end. Then we compute the transport at each time step and compare the full resolution model with the subsampled case. Doubling or halving the maximum strength of the jets or their propagation speed has no effect on our results.

With regards to the time-mean transport, we find that for regularly spaced sampling, 50 km resolution is sufficient to reproduce the transport within 2% of its true value, regardless of jet width. When the sampling is irregular and the spacing increased at the deeper end, mean transport predictions stay within 2–7% of their true value. However, if the jets are not allowed to migrate, but instead oscillate around the mean positions, transport errors increase to 10%.

In general, variability is overpredicted by the subsampled data, but correlations between the subsampled transport and the true transport are good (0.7 or higher) as long as the scale of the jets exceeds the sampling spacing. In cases when data spacing exceeds the jet-scale root mean square errors are comparable to those reported for the mean. When the spacing between observations is much larger than the jet width, the subsampled data have little skill to predict the time-varying transport. EOFs of the propagating jets, as for any propagating signal, show the signal spread out over a number of modes. Each mode captures a different phase of the propagation, and the associated PCs are correlated for a given lag. In the full resolution data the modes' spatial patterns are single-signed over one jet's width. When the jets are undersampled the anomalies captured by the EOF become wider than the jets width, since the EOF failed to resolve every phase of the propagation.

Acknowledgments
We thank Scott Worrilow and Brian Hogue, assisted by Jeff Pietro and Daniel Bogorff, for fielding the current meter instrumentation and moorings, Leah Trafford for processing the current meter records, Dan Torres for processing the moored ADCP record, and Mark Rosenberg and Serguei Sokolov for processing the CTD and LADCP data from the recovery cruise. We also thank the captain and crew of the Aurora Australis for their assistance during both the deployment and recovery cruises. The moored array data are archived at the U.S. National Oceanographic Data Center. The hydrographic data collected in support of the mooring operations are archived at the CLIVAR and Carbon Hydrographic Data Office. Surface geostrophic velocities produced by Ssalto/Duacs and distributed by Aviso can be obtained from http://www.aviso.altimetry.fr/duacs/. NCEP Reanalysis data was provided by the NOAA/OAR/ESRL PSD, Boulder, Colorado, USA, from their web site at http://www.esrl.noaa.gov/psd/. Bathymetric data at the mooring site were obtained from http://www.ibcso.org/. M.S.M. and the current meter array were supported by the National Science Foundation grant 0727045 "Measuring Westward Recirculation in the Subpolar Gyre of the Southeastern Indian Ocean." B.P.M. and S.R.R. were supported by the Cooperative Research Centre program of the Australian Government, through the Antarctic Climate and Ecosystems Cooperative Research Centre. S.R.R. was also supported by the Australian Government Department of the Environment, the Bureau of Meteorology and CSIRO through the Australian Climate Change Science Program. We would also like to thank Andy Thompson and one anonymous reviewer, as their comments greatly improved the manuscript.

References

Aoki, S., et al. (2007), A series of cyclonic eddies in the Antarctic Divergence off Adélie Coast, *J. Geophys. Res.*, *112*, C05019, doi:10.1029/2006JC003712.

Aoki, S., Y. Sasai, H. Sasaki, H. Mitsudera, and G. D. Williams (2010), The cyclonic circulation in the Australian–Antarctic Basin simulated by an eddy-resolving General Circulation Model, *Ocean Dyn.*, *60*(3), 743–757.

Arndt, J. E., et al. (2013), The International Bathymetric Chart of the Southern Ocean (IBSCO) version 1.0: A new bathymetric compilation covering circum-Antarctic waters, *Geophys. Res. Lett.*, *40*, 3111–3117, doi:10.1002/grl.50413.

Bindoff, N. L., M. A. Rosenberg, and M. J. Warner (2000), On the circulation and water masses over the Antarctic continental slope and rise between 80 and 150 E, *Deep Sea Res., Part II*, *47*(12), 2299–2326.

Dinniman, M. S., J. M. Klinck, and W. O. Smith (2011), A model study of Circumpolar Deep Water on the West Antarctic Peninsula and Ross Sea continental shelves, *Deep Sea Res., Part II*, *58*(13), 1508–1523.

Donohue, K. A., G. E. Hufford, and M. S. McCartney (1999), Sources and transport of the Deep Western Boundary Current east of the Kerguelen Plateau, *Geophys. Res. Lett.*, *26*(7), 851–854.

Fahrbach, E., M. Knoche, and G. Rohardt (1991), An estimate of water mass transformation in the Southern Weddell Sea, *Mar. Chem.*, *35*(1), 25–44.

Fukamachi, Y., et al. (2000), Seasonal variability of bottom water properties off Adélie Land, Antarctica, *J. Geophys. Res.*, *105*(C3), 6531–6540.

Fukamachi, Y., S. Rintoul, J. Church, S. Aoki, S. Sokolov, M. Rosenberg, and M. Wakatsuchi (2010), Strong export of Antarctic Bottom Water east of the Kerguelen Plateau, *Nat. Geosci.*, *3*(5), 327–331.
Garrett, C., P. MacCready, and P. Rhines (1993), Boundary mixing and arrested Ekman layers: Rotating stratified flow near a sloping boundary, *Annu. Rev. Fluid Mech.*, *25*(1), 291–323.
Gill, A. (1973), Circulation and bottom water production in the Weddell Sea, *Deep Sea Res. Oceanogr. Abstr.*, *20*(2), 111–140.
Gordon, A., D. Martinson, and H. Taylor (1981), The wind-driven circulation in the Weddell-Enderby Basin, *Deep Sea Res., Part A*, *28*(2), 151–163.
Gordon, A. L., A. H. Orsi, R. Muench, B. A. Huber, E. Zambianchi, and M. Visbeck (2009), Western Ross Sea continental slope gravity currents, *Deep Sea Res., Part II*, *56*(13), 796–817.
Heywood, K. J., R. A. Locarnini, R. D. Frew, P. F. Dennis, and B. A. King (1998), Transport and water masses of the Antarctic Slope Front System in the Eastern Weddell Sea, in *Ocean, Ice, and Atmosphere: Interactions at the Antarctic Continental Margin, Antarct. Res. Ser.*, vol. 75, edited by S. S. Jacobs and R. F. Weiss, pp. 203–214, AGU, Washington, D. C.
Heywood, K. J., M. D. Sparrow, J. Brown, and R. R. Dickson (1999), Frontal structure and Antarctic Bottom Water flow through the Princess Elizabeth Trough, Antarctica, *Deep Sea Res., Part I*, *46*(7), 1181–1200.
Jacobs, S. S. (1991), On the nature and significance of the Antarctic Slope Front, *Mar. Chem.*, *35*(1), 9–24.
Jacobs, S. S., A. Jenkins, C. F. Giulivi, and P. Dutrieux (2011), Stronger ocean circulation and increased melting under Pine Island Glacier ice shelf, *Nat. Geosci.*, *4*(8), 519–523.
Jensen, M. F., I. Fer, and E. Darelius (2013), Low frequency variability on the continental slope of the southern Weddell Sea, *J. Geophys. Res. Oceans*, *118*, 4256–4272, doi:10.1002/jgrc.20309.
Kalnay, E., et al. (1996), The NCEP/NCAR 40-year reanalysis project, *Bull. Am. Meteorol. Soc.*, *77*(3), 437–471.
Klatt, O., E. Fahrbach, M. Hoppema, and G. Rohardt (2005), The transport of the Weddell Gyre across the Prime Meridian, *Deep Sea Res., Part II*, *52*(3), 513–528.
MacCready, P., and P. B. Rhines (1991), Buoyant inhibition of Ekman transport on a slope and its effect on stratified spin-up, *J. Fluid Mech.*, *223*, 631–661.
McCartney, M. S., and K. A. Donohue (2007), A deep cyclonic gyre in the Australian–Antarctic Basin, *Prog. Oceanogr.*, *75*(4), 675–750.
Mathiot, P., H. Goosse, T. Fichefet, B. Barnier, and H. Gallée (2011), Modelling the seasonal variability of the Antarctic Slope Current, *Ocean Sci.*, *7*(4), 445–532.
Moffat, C., and S. Lentz (2012), On the response of a buoyant plume to downwelling-favorable wind stress, *J. Phys. Oceanogr.*, *42*(7), 1083–1098.
Morrow, R., G. Valladeau, and J.-B. Sallee (2008), Observed subsurface signature of Southern Ocean sea level rise, *Prog. Oceanogr.*, *77*(4), 351–366.
Nakayama, Y., K. I. Ohshima, Y. Matsumura, Y. Fukamachi, and H. Hasumi (2014), A numerical investigation of formation and variability of Antarctic Bottom Water off Cape Darnley, East Antarctica, *J. Phys. Oceanogr.*, *44*(11), 2921–2937.
Nøst, O., M. Biuw, V. Tverberg, C. Lydersen, T. Hattermann, Q. Zhou, L. Smedsrud, and K. Kovacs (2011), Eddy overturning of the Antarctic Slope Front controls glacial melting in the Eastern Weddell Sea, *J. Geophys. Res.*, *116*, C11014, doi:10.1029/2011JC006965.
Orsi, A., G. Johnson, and J. Bullister (1999), Circulation, mixing, and production of Antarctic Bottom Water, *Prog. Oceanogr.*, *43*(1), 55–109.
Orsi, A. H., T. Whitworth, and W. D. Nowlin (1995), On the meridional extent and fronts of the Antarctic Circumpolar Current, *Deep Sea Res., Part I*, *42*(5), 641–673.
Pritchard, H., S. Ligtenberg, H. Fricker, D. Vaughan, M. Van den Broeke, and L. Padman (2012), Antarctic ice-sheet loss driven by basal melting of ice shelves, *Nature*, *484*(7395), 502–505.
Purkey, S. G., and G. C. Johnson (2012), Global contraction of Antarctic Bottom Water between the 1980s and 2000s, *J. Clim.*, *25*(17), 5830–5844.
Shepherd, A., D. Wingham, and E. Rignot (2004), Warm ocean is eroding West Antarctic Ice Sheet, *Geophys. Res. Lett.*, *31*, L23402, doi:10.1029/2004GL021106.
Sokolov, S., and S. R. Rintoul (2002), Structure of Southern Ocean fronts at 140°E, *J. Mar. Syst.*, *37*(1), 151–184.
Speer, K. G., and A. Forbes (1994), A Deep Western Boundary Current in the South Indian Basin, *Deep Sea Res., Part I*, *41*(9), 1289–1303.
Stern, A., L.-P. Nadeau, and D. Holland (2015), Instability and mixing of zonal jets along an idealized continental shelf break, *J. Phys. Oceanogr.*, *45*(9), 2315–2338.
Stewart, A. L., and A. F. Thompson (2015), Eddy-mediated transport of Warm Circumpolar Deep Water across the Antarctic shelf break, *Geophys. Res. Lett.*, *42*, 432–440, doi:10.1002/2014GL062281.
St-Laurent, P., J. M. Klinck, and M. S. Dinniman (2013), On the role of coastal troughs in the circulation of Warm Circumpolar Deep Water on Antarctic shelves, *J. Phys. Oceanogr.*, *43*(1), 51–64.
Sun, C., and D. R. Watts (2001), A circumpolar Gravest Empirical Mode for the Southern Ocean hydrography, *J. Geophys. Res.*, *106*(C2), 2833–2855.
Tchernia, P., and P. Jeannin (1980), Observations on the Antarctic East Wind Drift using tabular icebergs tracked by satellite Nimbus F (1975–1977), *Deep Sea Res., Part A*, *27*(6), 467–474.
Thompson, A. F., and K. J. Heywood (2008), Frontal structure and transport in the northwestern Weddell Sea, *Deep Sea Res., Part I*, *55*(10), 1229–1251.
Thompson, A. F., K. J. Heywood, S. Schmidtko, and A. L. Stewart (2014), Eddy transport as a key component of the Antarctic Overturning Circulation, *Nat. Geosci.*, *7*(12), 879–884.
Wåhlin, A., O. Kalén, L. Arneborg, G. Björk, G. Carvajal, H. K. Ha, T. Kim, S. H. Lee, J. Lee, and C. Stranne (2013), Variability of warm deep water inflow in a submarine trough on the Amundsen Sea Shelf, *J. Phys. Oceanogr.*, *43*(10), 2054–2070.
Wakatsuchi, M., K. I. Ohshima, M. Hishida, and M. Naganobu (1994), Observations of a street of cyclonic eddies in the Indian Ocean sector of the Antarctic Divergence, *J. Geophys. Res.*, *99*(C10), 20,417–20,426.
Whitworth, T., A. Orsi, S.-J. Kim, W. Nowlin, and R. Locarnini (1998), Water masses and mixing near the Antarctic Slope Front, in *Ocean, Ice, and Atmosphere: Interactions at the Antarctic Continental Margin*, edited by S. S. Jacobs and R. F. Weiss, pp. 1–27, AGU, Washington, D. C.
Williams, G., S. Aoki, S. Jacobs, S. Rintoul, T. Tamura, and N. Bindoff (2010), Antarctic Bottom Water from the Adélie and George V Land Coast, East Antarctica (140–149°E), *J. Geophys. Res.*, *115*, C04027, doi:10.1029/2009JC005812.